Desalination and Water Treatment
www.deswater.com

doi: 10.5004/dwt.2018.23069

129 (2018) 116–126
October

Effects of spinning temperature on hollow fiber membrane prepared via thermally induced phase separation

Yajing Zhao[a,b,†], Chaohuan Yang[a,b,†], Lan Cheng[a,b], Juan Wang[c], Yingdong Li[a,b], Haoyun Wu[a,b], Pingli Li[a,b,*]

[a]*Chemical Engineering Research Center, School of Chemical Engineering and Technology, Tianjin University, Tianjin 300350, P.R. China, Tel. +86 22 27421723; emails: lipingli@tju.edu.cn (P. Li), chm.gold@163.com (Y. Zhao), 2515066790@qq.com (C. Yang), 1519146662@qq.com (L. Cheng), 676655086@qq.com (J. Wang), leeyd@126.com (Y. Li), 2539359136@qq.com (H. Wu)*
[b]*Tianjin State Key Lab of Membrane Science and Desalination Technology, Tianjin 300350, P.R. China*
[c]*WeiHai TuoZhan Fiber Company Limited, Shandong 264200, P.R. China*

Received 4 March 2018; Accepted 1 September 2018

ABSTRACT

In this study, isotactic polypropylene hollow fiber membranes were fabricated using co-diluent of di-n-butyl phthalate and dioctyl phthalate via thermally induced phase separation method. A coarsening model in terms of the momentum, mass and heat transfer during the spinning process was established to describe the effect of the spinning temperature on the membrane. The increasing spinning temperature increased the predicted solidification time and decreased phase separation time simultaneously. Moreover, the diluent evaporation on the outer surface is dramatically influenced by temperature. The prepared hollow fiber membranes were used to concentrate NaCl saline water of 30 up to 80 g/L about 100 h to evaluate the performance of air gap membrane distillation process in terms of permeation flux and gain output ratio. The salt rejection always exceeded 99.9% in the concentration experiment.

Keywords: Hollow fiber membranes; Thermally induced phase separation; Isotactic polypropylene; Air gap membrane distillation

1. Introduction

Hollow fiber membrane (HFM) with desirable separation properties has been widely used in innovation applications, ranging from bioseparation to water purification, gas separation, and bio-reactors [1–3]. HFM formed via thermally induced phase separation (TIPS) exhibits specific physicochemical characteristics and generally favorable surface area to volume ratio and mechanical properties [4,5]. Commercial HFM via TIPS is often made by dry-wet spinning process with the following steps: (1) preparing a homogeneous polymer solution with polymer solubilized in diluents at higher temperature, (2) inducing phase separation to evolve into polymer-lean and polymer-rich domains due to the effects of cooling medium (air or liquid quenching), (3) solidifying the polymer-rich phase and removing the diluents to yield a microporous structure [6–9].

The dry-wet spinning process of HFM is the transfer of mass, momentum, and heat simultaneously [4,10]. Spinning parameters are crucial factors that could have the influence on the membrane morphology and mechanical property, such as the type of polymer, diluent, spinning temperature, take-up velocity, the air-gap distance, and the core gas [4,11,12]. For a typical process, the extruded hollow fiber spinline tapers with an elevated axial velocity. Then, the spinline cools and solidifies with phase separation

* Corresponding author.

† These authors contributed equally to this work.

1944-3994/1944-3986 © 2018 Desalination Publications. All rights reserved.

as it passes through the air gap, and some diluents will be lost by evaporation [13]. Under these situations, evaporation and cooling will affect the concentration gradients and temperature profiles which is developing in the fiber. The elongation acts on the dimensions (inner and outer diameters), causing an indirect impact on the mass and energy transfer of the fiber [14,15].

Extensive experimental and theoretical studies have been devoted to the mechanisms of phase separation and to clarify the effect of various processing factors, including the effects of diluents, concentration, spinning temperature, quench temperature, as well as the air-cooling rate on the membrane morphologies [3,16–19]. Balasubramanian-Rauckhorst et al. [2] presented a model to predict extent of anisotropy in anisotropic HFM formation. Other models had been developed for HFM to clarify the correlation between spinning process and membrane properties [20–22]. The present work has been built on the thin filament analysis model [23] of the fiber spinning process. The steady-state behavior of the fiber spinning equations to material property and process variations were investigated. The local temperature of the spinline at the time of phase separation determines the kinetics involved in the phase separation process [2]. So it is important to clarify the phase separation and solidification while the spinline was elongated within the air gap. In the previous work [16], the effects of air-cooling on skin cells of HFM have been studied. In this paper, a mass and energy transfer model was presented to provide some insight into the velocity, temperature profiles, and diluents evaporation in the axial dimension with different spinning temperatures. The model has also been used to improve the understanding of the correlation between the phase separation and the HFM properties. To validate the theoretical results, we used a system consisting of isotactic polypropylene (iPP) and the co-diluent of di-n-butyl phthalate (DBP) and dioctyl phthalate (DOP) to prepare hollow-fiber asymmetric membrane. Moreover, the prepared membranes were tested to concentrate NaCl saline water through air-gap membrane distillation (AGMD) process lasting 100 h.

2. Spinning process model

Assumptions have been taken into consideration as the following: (1) no draw-down or gravity is exerted on the fiber and that inertia could be neglected. (2) The dimensions of the fiber are constant in the spinning process. (3) Mass and heat transfer take place simultaneously.

Fig. 1 shows a process of an extruding hollow fiber. The TIPS occurs in the draw zone (from $z = 0$ to $z = L$), where the membrane structure and properties are determined. The HFM solidify at the point $z = L$, at which the membrane morphologies would have no obvious change. So we define the point $z = L$ as the solidification point, where the T(L) is the crystallization temperature of the spinning polymer solution. Axial velocity v_z(L) is the take-up speed.

The equation of continuity, the ideal gas law and axial velocity are given without derivation in Eqs. (1)–(3) as found in the literature [23]. All equations presented here are for a steady-state operation:

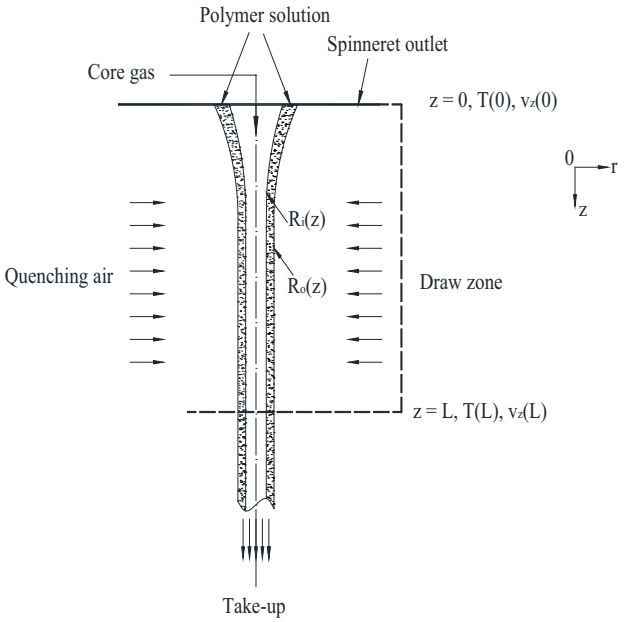

Fig. 1. Process of an extruding hollow fiber.

$$\left(\frac{R_o}{R_i}\right)^2 = 1 + \frac{\rho_i w_o}{\rho_o w_i} = R_o^2\left(\frac{\pi v_z \rho_i}{w_i}\right) \tag{1}$$

$$\rho_i = \frac{\left(\bar{P}_i + P_{\text{atm}}\right) M_i w_i}{RT} \tag{2}$$

$$v_z = v_z(0)\left[\frac{v_z(\text{L})}{v_z(0)}\right]^{\frac{z}{L}} \tag{3}$$

where R_o (mm) and R_i (mm) are outer and inner radii of spinline; v_z (m/s) is the spinline axial velocity; ρ_0 (kg/m^3) and ρ_i (kg/m^3) represent spinline and core gas densities; w_0 (kg/s) and w_i (kg/s) are the mass flow rates of spinline and core gas; $\bar{P}_i$ (kPa) is the core gas gauge pressure at a given axial position; P_{atm} (kPa) is the ambient air pressure; M_i is the core gas molecular weight; R is the universal gas constant; and T (K) represents the cross-sectional average spinline temperature at a given axial position z (m).

Mass transfer and heat transfer are assumed to take place simultaneously. Cooling of the nascent hollow fiber occurs simultaneously with evaporation of the diluents only from the skin of the hollow fiber, as well as the diluents without axial diffusion. In addition, the system is incompressible and the fiber is axisymmetric. Transient mass transfer of the volatile component in the system is described as follows:

$$v_z \frac{\partial C_d}{\partial z} = D\frac{1}{r}\frac{\partial}{\partial r}\left(r\frac{\partial C_d}{\partial r}\right) \tag{4}$$

where r (m) is the radial position of cross-sectional structure; C_d is the mass fraction of the volatile component in the dope;

and D (cm²/s) is the diffusion coefficient of the volatile component.

In this work, a skin-free asymmetric membrane with a porous sublayer was prepared via TIPS. The thickness of the sublayer was less than 1 μm (ε ≤ 1 μm).

Boundary conditions are described as follows:

$$\begin{cases} r = R_o: & -D\left.\dfrac{\partial C_d}{\partial r}\right|_{R_o} = k_c\left(C_d^g\big|_{R_o} - C_d^g\big|_{\infty}\right) \\ r = R_o - \varepsilon: & -D\left.\dfrac{\partial C_d}{\partial r}\right|_{R_o-\varepsilon} = 0 \end{cases} \tag{5}$$

here k_c is the convective mass transfer coefficient (m/s); $C_d^g\big|_{\infty}$ is the vapor mass fraction of the volatile component at infinity, and assumed to be zero. The thickness of the sublayer ε is much less than the radius of HFM (R_o). Thus, the concentration of diluents (C_d) in the bulk of the drop cross-section is assumed to be the same, and only varies in the axial dimension.

$C_d^g\big|_{R_o}$ is the vapor mass fraction of the volatile component near the outer surface, and expressed as follows [2]:

$$C_d^g\big|_{R_o} = \frac{p_d^o M_d}{RT}\left(\phi_d\big|_{R_o}\right)\exp\left[1-\phi_d\big|_{R_o} + \chi\left(1-\phi_d\big|_{R_o}\right)^2\right] \tag{6}$$

$$C_d = \rho_d^0 \phi_d \tag{7}$$

where p_d^o (kPa) is the vapor pressure of the volatile component; M_d is the molecular weight of the volatile component; R is the ideal gas constant; ϕ_d is the volume fraction of the volatile component in the dope and χ is the interaction parameter; ρ_d^0 (kg/m³) is the density of the diluents.

$$v_z\left(2R_o\varepsilon - \varepsilon^2\right)\rho_d^0\frac{d\phi_d}{dz} = -2R_o k_c \frac{p_d^o M_d}{RT}\phi_d \exp\left[1-\phi_d + \chi\left(1-\phi_d\right)^2\right] \tag{8}$$

which is the final form of the mass transfer equation.

The general form of the energy balance that applies at the drop-air quench interface is given as Eq. (9) [23]:

$$\left(w_o C_{\mathrm{po}} + w_i C_{\mathrm{pi}}\right)\frac{dT}{dz} = -2\pi R_o h\left(T - T_q\right) \tag{9}$$

where C_{po} (kJ/(kg·K) and C_{pi} (kJ/(kg·K) are spinline and core gas heat capacities; h (W/(m²·K)) is the convective heat transfer coefficient, T_q (K) is the temperature of the quenching air. At $r = R_o$, the heat consists of convective heat transfer and heat loss resulting from evaporation of the diluents, that is:

$$-k_o\left.\frac{\partial T_o}{\partial r}\right|_{r=R_o} = h\left(T_o\big|_{r=R_o} - T_q\right) + \Delta H_d^{\mathrm{vap}} j \tag{10}$$

where $\Delta H_d^{\mathrm{vap}}$ (J/g) is the evaporation enthalpy of the diluents; j is the evaporation flux of the diluents. With the boundary conditions (Eq. (10)), the axial energy balance is given as Eq. (11):

$$\left(w_o C_{\mathrm{po}} + w_i C_{\mathrm{pi}}\right)\frac{dT}{dz} = -2\pi R_o\left[h\left(T - T_q\right) + \Delta H_d^{\mathrm{vap}} j\right] \tag{11}$$

And the Fick's law:

$$j = -D\frac{\partial C_d}{\partial r} \tag{12}$$

Substituting Eqs. (5), (7) and (12) into (11) gives the final axial energy balance equation, which can be used to model the axial temperature profile of HFM:

$$\left(w_o C_{\mathrm{po}} + w_i C_{\mathrm{pi}}\right)\frac{dT}{dz} = -2\pi R_o \left[h\left(T - T_q\right) + \Delta H_d^{\mathrm{vap}} k_c \frac{p_d^o M_d}{RT}\phi_d \exp\left(1-\phi_d + \chi\left(1-\phi_d\right)^2\right)\right] \tag{13}$$

3. Experimental setup

3.1. Membrane preparation

For membrane preparation, iPP (Daqing Petroleum Chemical, China), DOP and DBP (Tianjin Bodi Chemical Reagents, China) were used to prepare the extruding dope, in which iPP was 26 wt %, and DBP in the co-diluent was 35 wt %; Petroleum ether (Tianjin Bodi Chemical Reagents, China) was used as extractant. All materials were used without any further treatment.

To obtain the effects of spinning temperature on HFM, the components iPP, DBP, and DOP were heated in a dasher to form a homogeneous solution. The dope was extruded from the spinneret with nitrogen as core gas. Through the pull of the take-up drum, the nascent hollow fiber passed through an air quencher where phase separation occurred, and the length of the air gap was 0.2 m. Subsequently, the hollow fibers were removed from the take-up drum, immersed in petroleum ether for 12 h to extract the diluents, and then air-dried.

For the iPP-DOP-DBP system, the homogeneous solution started to evolve into two phases (polymer-rich matrix phase and diluent-rich droplets) when it was cooled to a temperature (liquid–liquid phase separation occurs at 407.5 K) below the spinodal line, through the spinodal decomposition mechanism; then the droplets grew until the mixture reached the crystallization curve temperature (379.5 K), at which point the polymer-rich matrix solidified [24,25].

As discussed in previous work [16], during spinning process, quenching occurred simultaneously with evaporation of the diluents from the skin. The vapor pressure of DBP was much higher than that of DOP during the temperature of 396.15 K~434.15 K. Thus, the main volatile component was expected to be DBP.

3.2. Characterization of the HFM

The HFM was fractured in liquid nitrogen and coated with gold. A scanning electron microscope (SEM XL30, Philips, Hitachi Ltd., Tokyo, Japan) with an accelerating voltage of 20 kV was used to examine the morphology of the cross-section and outer surface of membranes.

Membrane pore parameters such as average pore size and pore size distribution were determined by membrane pore size analyzer (3H-2000PB, BeiShiDe Instrument Technology, Beijing, China).

The membrane porosity (ε) was measured by gravimetric method:

$$\varepsilon = \frac{m_1 - m_2}{\rho \Delta V_m} \tag{14}$$

where m_1 is the mass of the wet membrane (g), m_2 is the mass of dry membrane (g), ρ is the density of absolute ethyl alcohol (0.79 g/mL), ΔV_m is the apparent volume of the membrane. All tests were repeated for three times to get mean values.

4. Results and discussion

4.1. Physical parameters

The heat transfer coefficient h is taken from the literature [26] as shown in Eq. (15). This relationship takes into account the physical properties of the quenching air and the values for air as given in Eqs. (16)–(18):

$$h = 0.42\left(\frac{k_q}{2R_o}\right)\left(\frac{2\rho_q v_z R_o}{\eta_q}\right)^{1/3}\left[1+\left(\frac{8v_q}{v_z}\right)^2\right]^{1/6} \tag{15}$$

$$\rho_q = 2.41 - 3.58\times10^{-3}T_q \tag{16}$$

$$\eta_q = 4.29\times10^{-6} + 4.75\times10^{-8}T_q \tag{17}$$

$$k_q = 4.36\times10^{-3} + 7.27\times10^{-5}T_q \tag{18}$$

where ρ_q (kg/m^3) is the density, k_q (W/(m^2·K)) is the thermal conductivity, η_q (Pa·s) is the viscosity, and T_q (K) is the temperature of quenching air.

The convective mass transfer coefficient k_c (m/s) is estimated from the following formulas (Eq. (19)), where D_{d-air} (K) represents the coefficient for diffusion of the diluent DBP into air, which is expressed as a function of T.

$$k_c = \frac{RT_q}{p_{atm}}\left(\frac{\rho_q D_{d-air}}{k_q C_{p,q}}\right)^{\frac{1}{2}}\frac{h}{M_q} \tag{19}$$

$$D_{d-air} = -6.84\times10^{-6} + 3.67\times10^{-8}T \tag{20}$$

where $C_{p,q}$ (kJ/(kg·K)) is the specific heat at constant pressure of air, and M_q is the molecular weight of the air. Other system physical properties for the base case are list in Tables S1 and S2.

4.2. Predicted effects of spinning temperature on HFM

Fig. 2 shows the axial velocity curves of the spinline at different temperatures. The curves for the three cases show the same trend, increasing monotonically along the draw zone, as the velocities for the three cases converge to the identical take-up velocity. In addition, higher initial spinning temperature corresponds to lower spinline velocity and longer draw zone length (L). That is, there is a lower velocity gradient of the spinline, which behavior is the consequence of the change in axial stress with spinline cooling. Since the axial stress in the spinline correlates with molecular orientation [27], and smaller axial stress growth contributes to the membrane stability [28], thus, higher temperature is conducive to the experimental work on the spinning process conditions.

In order to predict the phase separation of the spinline in the draw zone, the predicted spinline temperature profiles (Fig. 3) have nearly identical trends. The final fiber temperature at the end of the draw zone is the crystallization

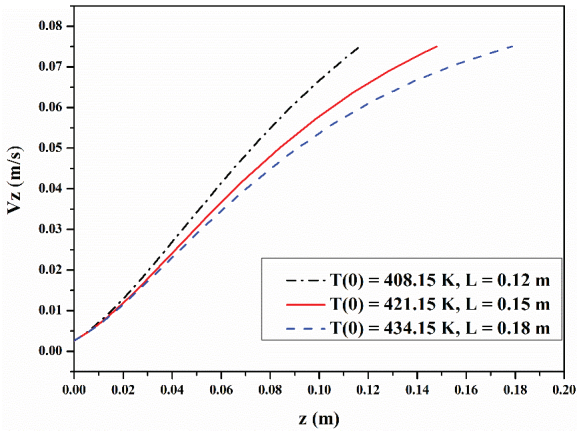

Fig. 2. Effects of spinning temperature on spinline axial velocity.

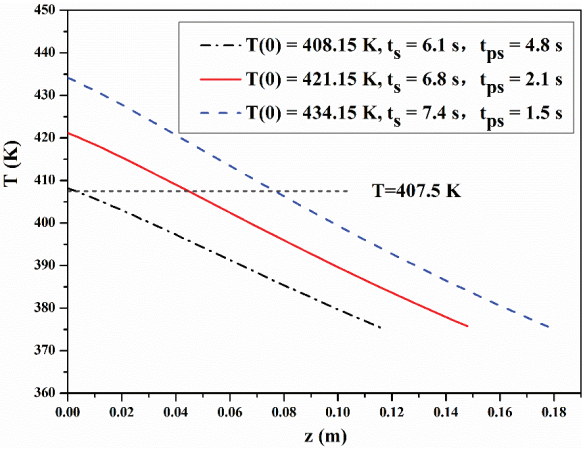

Fig. 3. Effect of spinning temperatures on spinline axial temperature.

temperature. At this point, elongation of the spinline stops, and the final value of spinline diameter is reached, essentially restricting the draw zone. As it shown, higher initial spinning temperatures correspond to higher temperatures throughout the draw zone. In addition, it will take longer time for phase separation beginning induced by cooling the polymer solution at higher spinning temperature, also with longer solidification time t_s. Therefore, it will increase the heat loss, maybe even if slightly. Results in Figs. 2 and 3 show that the spinline undergoes phase separation with a faster axial velocity, which leads to shorter phase separation time t_{ps} with relatively convective heat transfer enhancement. Therefore, it will decrease the time for diluent-rich droplets growing, changing the magnitude of the droplets gradient over the cross-sectional spinline. However, the sizes of the diluent-rich domains in the phase-separated spinline relate directly to the pore sizes of the final membrane [29]. Thus, control of the spinning temperature that affects the size of these domains before phase separation occurs is important to control the membrane microstructure.

The loss rate of DBP at the outer surface of spinline presented in Fig. 4 reflects significant changes with the variations of temperatures. The differences in predicted spinning temperature among the cases with the different predicted spinline velocity create a dissimilarity of diluent volatility, which affect diluent evaporation rate at the spinline outer surface. It can be found that high rates of mass transfer as diluent evaporates very quickly at higher spinning temperature leading to high rates of heat transfer at axial position in the draw zone, which will result in diluent-rich droplets diminishing. Thus, for the HFM spinning conditions simulated here, spinning temperature has been proven to have a significant effect on the loss rate of DBP, an important consideration in terms of membrane morphology.

4.3. Morphologies of the HFM

Fig. 5 presents the effect of spinning temperatures (from 418.15 to 434.15 K) on membrane morphology. The cross-sections for the three cases show a similar bicontinuous structure, while, the pore sizes decrease to some extent.

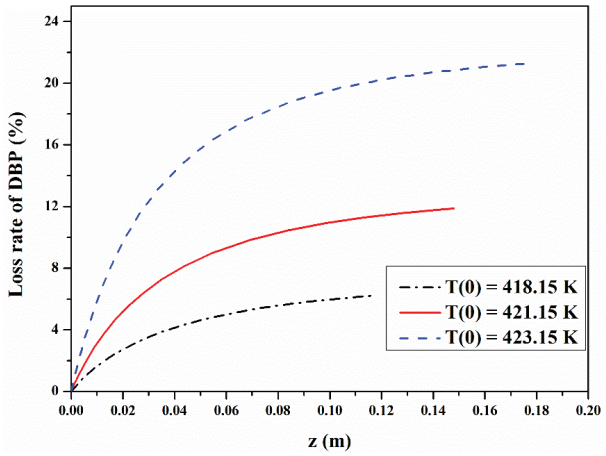

Fig. 4. Effect of spinning temperatures on DBP loss rate at the outer surface.

The pore sizes are on average smaller near the outer skin, resulting from diluent evaporation in this region during spinning process. The results are equivalent to the analysis that discussed above for the temperature studies of Figs. 3 and 4. On the membrane surfaces, there is a skin-free layer with porous structure formed. Moreover, there is the biggest pore size on the surface for the 421.15 K spinning case. The cause of the discrepancy is the existence of two competing effect of viscosity with a stronger dependence on temperature and diluent volatile quantity on the membrane extent of anisotropy. Smaller pores are formed due to the restricted droplet coalescence by the higher viscosity in lower temperature in the skin layer; as temperature rising, bigger pores are formed due to reduced viscosity and enhanced diluent evaporation; at the highest temperature, the dominant diluent evaporation led to pores diminishing. The results have been verified further by the data in Fig. S1 and Table 1, which membranes prepared at 421.15 K had relatively higher porosity.

4.4. NaCl saline water concentration experiment

In order to test the HFM, 30 g/L NaCl saline water was concentrated by AGMD using HFMs which were fabricated under 421.15 K. The net-hollow fiber membranes-net-dense-wall hollow fibers four-layer sheet is rolled up tightly and the net between the membranes and the dense-wall hollow fibers was used to fix the gap width. Then the sheet was placed in an ABS tube and two edges of the tube were sealed by epoxy resin. In the end, the HFMs and dense-wall hollow fibers were cut open at both ends to accommodate the feed channel. The membrane module parameters are listed in Table 2.

The concentration experimental system of AGMD is shown in Fig. 6. During the experiment, the 30°C preheating NaCl saline water was first pumped into the dense-wall hollow fiber channel at the bottom of the AGMD module, after recovering the latent heat, the saline water flowed into the thermostat B where it was heated to 80°C. Then the hot saline water was pumped into the inlet of HFMs at the top of the AGMD module, the concentrated saline water out from the bottom of HFM channel flowed back into the thermostat A. The temperatures of inlets and outlets of feed and coolant (T_1, T_2, T_3, and T_4) were monitored by thermocouples. The feed flow rates in two channels were 10 L/h adjusting by two rotameters. The water produced was collected and conductivity was recorded every 10 min after the system ran stably.

The water flux, J, and gain output ratio, GOR, which can be considered to be energy recovery efficiency, were calculated by the following equations:

$$J = \frac{V}{\Delta t \times A} \tag{21}$$

$$\mathrm{GOR} = \frac{V \Delta H}{F \rho C_p (T_3 - T_2)} \tag{22}$$

where V means the value of produced water (L), A is the effective membrane area (m^2), Δt means the operation time (h).

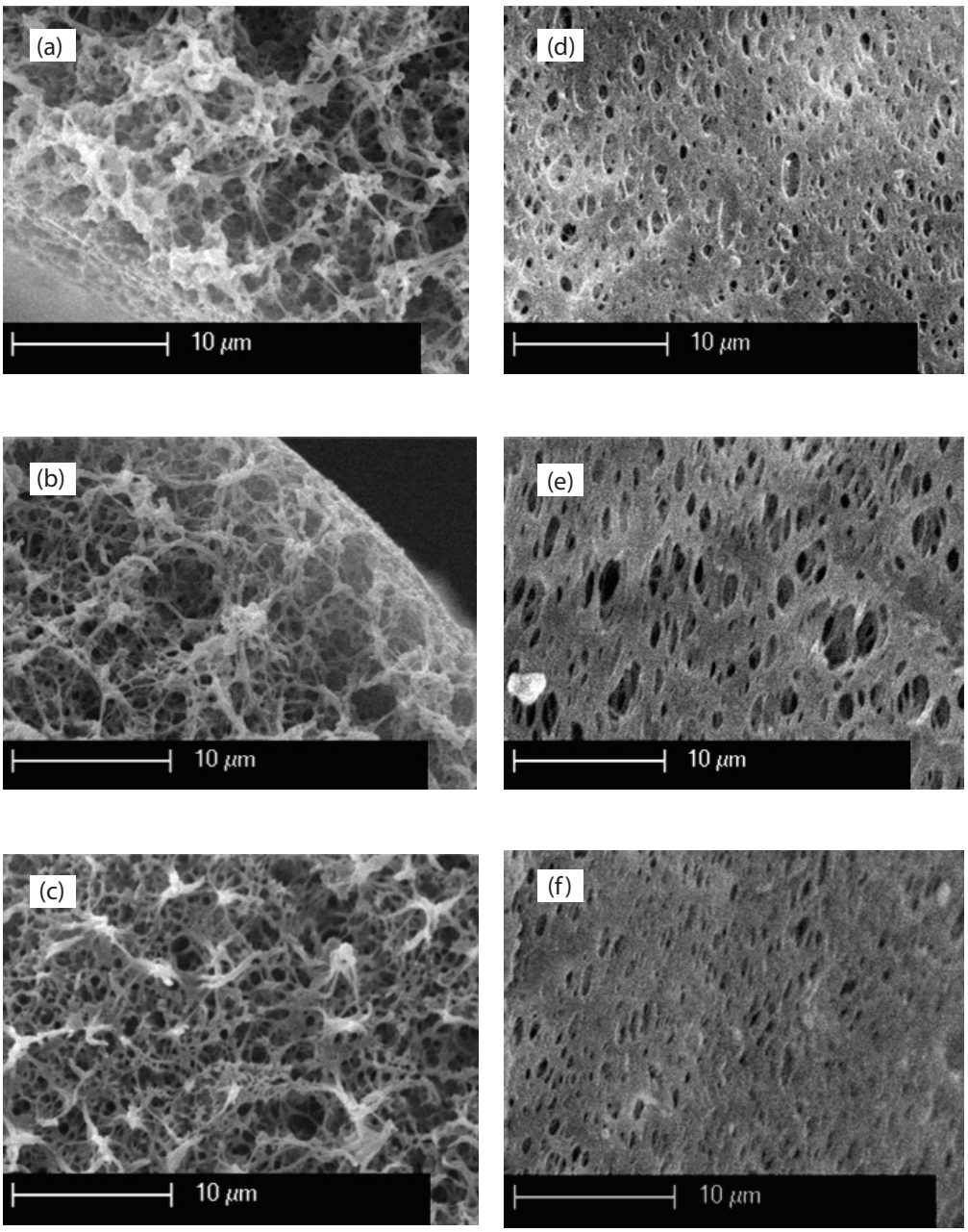

Fig. 5. Effect of spinning temperatures on membrane morphology. (a) $T(0)$ = 408.15 K cross-section 2,000×, (b) $T(0)$ = 421.15 K cross-section 2,000×, (c) $T(0)$ = 434.15 K cross-section 2,000×, (d) $T(0)$ = 408.15 K outer 2,000×, (e) $T(0)$ = 421.15 K outer 2,000×, (f) $T(0)$ = 434.15 K outer 2,000×.

Table 1
Membrane pore parameters of average pore size and porosity

	408.15 K	421.15 K	434.15 K
Average pore size (μm)	0.322	0.398	0.311
Porosity (%)	67.7	69.1	65.1

ΔH is the enthalpy of water evaporation (J/kg), F is the flow rate of feed (L/h), ρ is the density of produced water (kg/L), C_p means the specific heat of feed (J/kg°C), T_3 and T_2 are the temperatures of feed inlets and coolant outlets, respectively.

Fig. 7 shows J and GOR in continuous concentration of 30 g/L NaCl saline water. In the first test lasting 72 h, J and GOR decreased by 36.7% and 59.4%, respectively, then the pure water was used to clean the membrane module about 5 h. After rinsing the membrane module, J and GOR recovered to 77% and 64% of the initial level, then the less concentrated solution (58.4 g/L) was still used to test the HFMs in the second test.

J decreased obviously in the two membrane concentration tests, there are two major factors which have influence on the flux. One is salinity, the other is crystals adhering to the membrane. First, we investigated the effect of the salinity

on the flux. The water flux can be estimated by the mass transfer model as Eq. (23):

$$J = K_m \times \left(p_{hm} - p_{pm}\right) \tag{23}$$

where K_m (L/m²·h·Pa) is membrane distillation coefficient which is related to membrane properties, P_{hm} (Pa) and P_{pm} (Pa) are the partial pressures of water vapor pressure at the lumen side of membrane surface and that at the surface of the shell side, respectively. P_{pm} is actually vapor pressure of water when permeate is nearly pure water.

Water vapor pressure of NaCl saline water can be defined by:

$$P(T,x) = P^*(T)a_w(x) \tag{24}$$

where T (K) means saline water temperature, x is NaCl solution mole fraction, $a_w(x)$ is water activity of saline water, which means the ratio between water vapor of the saline water to the pure water vapor pressure at the same temperature, $P^*(T)$ (Pa) is the pure water vapor pressure at a saline water temperature which can be calculated by Antoine equation:

$$P \times (T) = \mathrm{Exp}\left(23.238 - \frac{3841}{T - 45}\right) \tag{25}$$

The water activity of NaCl saline water [30] can be calculated by Eq. (26):

$$a_w\left(x\right) = (1-x)\mathrm{Exp}(1.825x^2 - 20.78x^3) \tag{26}$$

According to Eqs. (24)–(26), salinity can affect water vapor pressure and water activity obviously. Fig. 8(a) shows that when the saline water was concentrated, the water

Table 2
Major parameters of the module

Parameters	Value
Membrane average pore size(μm)	0.39
Membrane porosity (%)	69.1
Water contact angle (°)	109
Liquid entrance pressure (MPa)	0.14
Membrane outer diameter (mm)	0.6
Membrane inner diameter (mm)	0.44
Dense-wall hollow fiber outer diameter (mm)	0.5
Dense-wall hollow fiber inner diameter (mm)	0.4
Gap thickness (mm)	0.5
Effective length (m)	0.4
Shell inner diameter (mm)	42
Number of hollow fiber membrane	180
Number of dense-wall hollow fiber	360
Total membrane surface area (m²)	0.0995

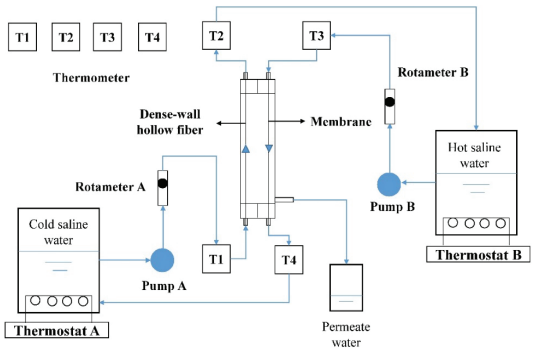

Fig. 6. Schematic diagram of AGMD experimental set-up.

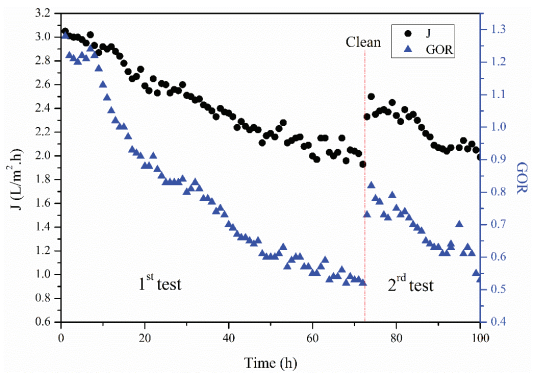

Fig. 7. AGMD concentration experiment performance.

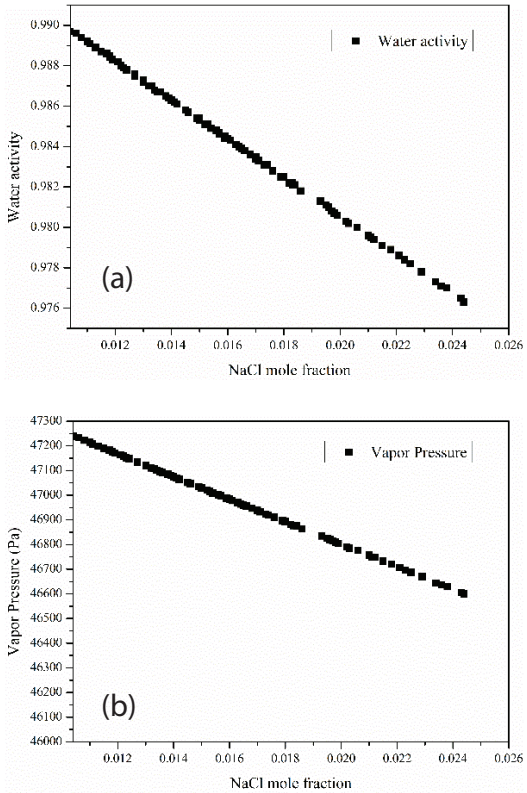

Fig. 8. Effect of concentration on (a) the water activity and (b) the water vapor pressure of NaCl saline water.

activity reduced significantly, which caused decreasing water vapor pressure of NaCl saline water. Fig. 8(b) shows the effect of saline water concentration on water vapor pressure. *J* is related to the water vapor pressure differences on the membrane, the higher the concentration of saline water, the lower water vapor pressure of feed, which caused lower trans-membrane vapor pressure differences in Eq. (23), and thereby reduced mass transfer driving force. So with the increasing salinity, *J* decreased in the whole concentration experiment. Moreover, the maximal flux after rinsing in the second test could not recover to the initial level in the first test, which is shown in Fig. 7.

Meanwhile, the crystals adhering to the inner membrane surface also caused declined flux. After the second test, the prepared and used HFMs were examined using the SEM and the SEM images are shown in Fig. 9. Compared with the prepared laboratorial HFM, the used membrane inner surface was partially covered by fouling deposits. In this case, the blockage of open pore area caused by crystallization on the membrane increased resistance of mass transfer and led to the reduction of *J*. However, the NaCl crystals did not appear in the cross-sectional SEM images of used membrane, which means that scaling occurred on the inner membrane surface and the NaCl crystals did not block the pores in the internal membrane.

Because of two reasons mentioned above, *J* declined in the experiment, which led to lower latent heat which the trans-membrane vapor carried, so more external heat source

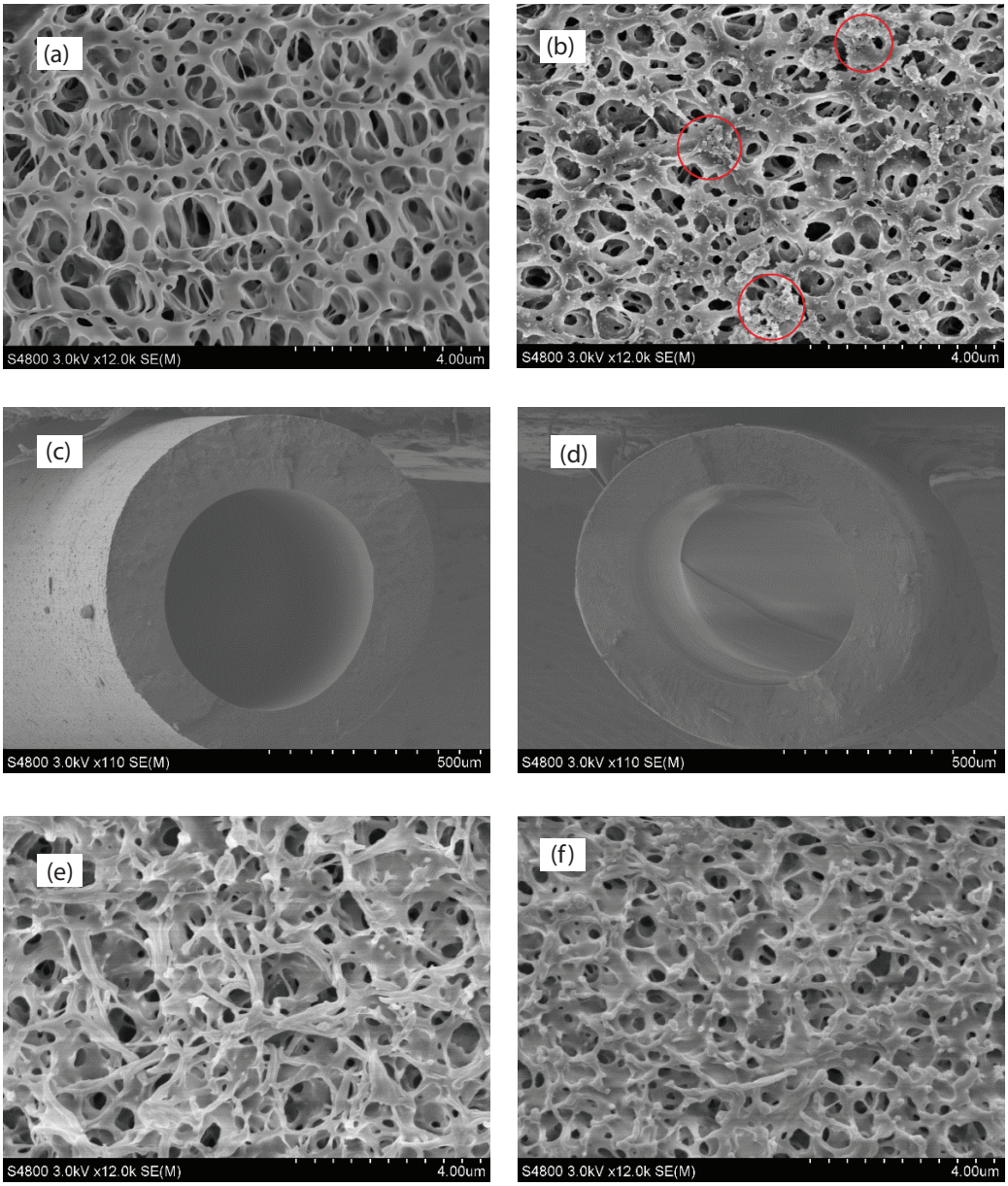

Fig. 9. SEM images: (a) the inner surface of prepared membrane, (b) the inner surface of fouled membrane, (c) the cross-section of prepared membrane, (d) the cross-section of fouled membrane, (e) the enlarged cross-section of prepared membrane, (f) the enlarged cross-section of fouled membrane.

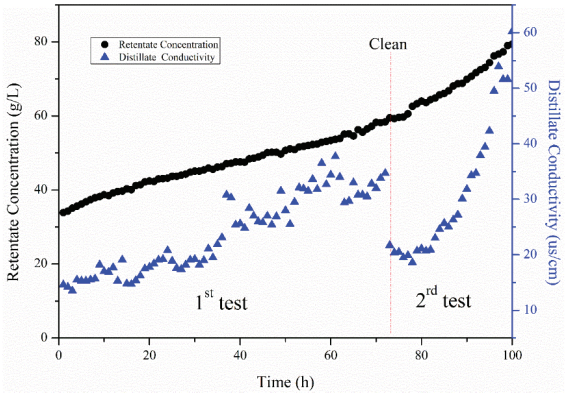

Fig. 10. Retentate concentration and the distillate conductivity with time during membrane concentration experiment.

was required to provide more heat to maintain the hot feed temperature constant, resulting in the decrease of GOR with the concentration of the NaCl saline water (Fig. 7).

Fig. 10 shows the retentate concentration and the distillate conductivity during membrane concentration experiment. In the first test, the retentate concentration increased slowly because the distillate volume was small comparing with the retentate volume. However, the magnitude of the retentate volume decrease was greater than the magnitude of the drop in distillate volume in the second test, so the retentate concentration increased more rapidly.

The distillate conductivity increased as the membrane concentration experiment going on, this could be estimated that crystals formed on the inner membrane surface caused little membrane wetting and deteriorated the water quality. In the beginning of the second test, the distillate conductivity decreased significantly because NaCl crystals accumulated on the membrane surface were eliminated by the rinsing measure. The maximum distillate conductivity in the whole experiment was lower than 60 μS/cm, which means that the salt rejection always exceeded 99.9%. This indicated that laboratorial HFMs can be used for concentrating saline water, but some cleaning measurements to reduce the effect of fouling on the process performance are still required.

5. Conclusions

In this work, a new coarsening model was conducted to investigate the effects of spinning temperature on axial velocity, temperature profiles and the loss rate of DBP on the outer surface of the spinline in the air gap region during membrane spinning process of the polymer-diluent system via TIPS. The results proved that spinning temperature has significant influences on the membrane. The cross-sectional morphology of the prepared membranes exhibit symmetrical bicontinuous structure and skin-free layer forms on the outer surface. The decrease of viscosity in spinline brought on by increasing spinning temperatures can be beneficial to the droplets growing. But the droplets could be to a lesser extent due to the shorten phase separation time and larger diluent evaporation, which could tune the pore size in the final fiber. The AGMD concentration process was carried out in the NaCl saline water to test the membrane. J and GOR decreased because of increasing salinity and some crystals formed on the inner membrane surface. However, the salt rejection always exceeded 99.9% in the concentration experiment, which means that the membrane can be used to concentrate the NaCl solution.

Symbols

A	—	Membrane area, m^2
C_d	—	Mass fraction of the volatile component in the dope
C_{po}	—	Heat capacity of spinline, kJ/(kg·K)
C_{pi}	—	Heat capacity of core gas, kJ/(kg·K)
D	—	Diffusion coefficient of the volatile component, cm^2/s
GOR	—	Gain output ratio
ΔH	—	Enthalpy of water evaporation, J/kg
J	—	Water flux, L/(m^2•h)
k_q	—	Thermal conductivity, W/(m^2·K)
T	—	Temperature, °C
v_z	—	Spinline axial velocity, m/s
z	—	Spinline axial position, m
ϕ_d	—	Volume fraction of the volatile component in the dope
η_q	—	Viscosity, Pa·s
χ	—	Interaction parameter
ρ_i	—	Core gas density, kg/m^3
ρ_o	—	Spinline density, kg/m^3

References

[1] J.V. Alexander, J.W. Neely, E.A. Grulke, Effect of chemical functionalization on the mechanical properties of polypropylene hollow fiber membranes, J. Polym. Sci. Part B Polym. Phys., 52 (2014) 1366–1373.
[2] H.A. Balasubramanian-Rauckhorst, D.R. Lloyd, G.G. Lipscomb, Predicting extent of anisotropy in anisotropic hollow fiber membrane formation, J. Membr. Sci., 339 (2009) 250–260.
[3] W. Yave, R. Quijada, M. Ulbricht, R. Benavente, Syndiotactic polypropylene as potential material for the preparation of porous membranes via thermally induced phase separation (TIPS) process, Polymer, 46 (2005) 11582–11590.
[4] C.Y. Feng, K.C. Khulbe, T. Matsuura, A.F. Ismail, Recent progresses in polymeric hollow fiber membrane preparation, characterization and applications, Sep. Purif. Technol., 111 (2013) 43–71.
[5] B. Luo, Z. Li, J. Zhang, X. Wang, Formation of anisotropic microporous isotactic polypropylene (iPP) membrane via thermally induced phase separation, Desalination, 233 (2008) 19–31.
[6] H.Q. Liang, Q.Y. Wu, L.S. Wan, X.J. Huang, Z.K. Xu, Polar polymer membranes via thermally induced phase separation using a universal crystallizable diluent, J. Membr. Sci., 446 (2013) 482–491.
[7] M.E. Vanegas, R. Quijada, D. Serafini, Microporous membranes prepared via thermally induced phase separation from metallocenic syndiotactic polypropylenes, Polymer, 50 (2009) 2081–2086.
[8] H. Matsuyama, M.-m. Kim, D.R. Lloyd, Effect of extraction and drying on the structure of microporous polyethylene membranes prepared via thermally induced phase separation, J. Membr. Sci., 204 (2002) 413–419.
[9] Q.Y. Wu, L.S. Wan, Z.K. Xu, Structure and performance of polyacrylonitrile membranes prepared via thermally induced phase separation, J. Membr. Sci., 409–410 (2012) 355–364.
[10] Z. Gou, A.J. McHugh, A comparison of Newtonian and viscoelastic constitutive models for dry spinning of polymer fibers, J. Appl. Polym. Sci., 87 (2003) 2136–2145.

[11] N. Peng, N. Widjojo, P. Sukitpaneenit, M.M. Teoh, G.G. Lipscomb, T.-S. Chung, J.-Y. Lai, Evolution of polymeric hollow fibers as sustainable technologies: past, present, and future, Prog. Polym. Sci., 37 (2012) 1401–1424.
[12] T.S. Chung, Z.L. Xu, W. Lin, Fundamental understanding of the effect of air-gap distance on the fabrication of hollow fiber membranes, J. Appl. Polym. Sci., 72 (1999) 379–395.
[13] V. Simon, The temperature of fibers during air-gap wet-spinning: cooling by convection and evaporation, Int. J. Heat Mass Trans., 37 (1994) 1133–1142.
[14] T.S. Chung, The limitations of using Flory-Huggins equation for the states of solutions during asymmetric hollow-fiber formation, J. Membr. Sci., 126 (1997) 19–34.
[15] J. Yin, N. Coutris, Y. Huang, Role of Marangoni instability in fabrication of axially and internally grooved hollow fiber membranes, Langmuir, 26 (2010) 16991–16999.
[16] H. Wu, L. Li, P. Li, Q. Yin, H. Chang, Effects of air-cooling on skin cells of hollow-fiber membranes prepared via thermally induced phase separation, Polym. Eng. Sci., 55 (2015) 1661–1670.
[17] Y. Mino, T. Ishigami, Y. Kagawa, H. Matsuyama, Three-dimensional phase-field simulations of membrane porous structure formation by thermally induced phase separation in polymer solutions, J. Membr. Sci., 483 (2015) 104–111.
[18] H. Matsuyama, M. Yuasa, Y. Kitamura, M. Teramoto, D.R. Lloyd, Structure control of anisotropic and asymmetric polypropylene membrane prepared by thermally induced phase separation, J. Membr. Sci., 179 (2000) 91–100.
[19] N. Widjojo, T.S. Chung, Thickness and air gap dependence of macrovoid evolution in phase-inversion asymmetric hollow fiber membranes, Ind. Eng. Chem. Res., 45 (2006) 7618–7626.
[20] S.J. Shilton, Forced convection spinning of hollow fibre membranes: modelling of mass transfer in the dry gap, and prediction of active layer thickness and depth of orientation, Sep. Purif. Technol., 118 (2013) 620–626.
[21] V. Simon, Analysis of fiber formation during air-gap wet spinning, AIChE J., 41 (1995) 1281–1294.
[22] T.S. Chung, X. Hu, Effect of air-gap distance on the morphology and thermal properties of polyethersulfone hollow fibers, J. Appl. Polym. Sci., 66 (1997) 1067–1077.
[23] G.G. Lipscomb, The melt hollow fiber spinning process: steady-state behavior, sensitivity and stability, Polym. Adv. Technol., 5 (1994) 745–758.
[24] Z.S. Yang, Studies on Preparation and Morphology Controlling of iPP Hollow Fiber Microporous Membrane via Thermally Induced Phase Separation, Tianjin University, 2005.
[25] Y.K. Lin, G. Chen, J. Yang, X.L. Wang, Formation of isotactic polypropylene membranes with bicontinuous structure and good strength via thermally induced phase separation method, Desalination, 236 (2009) 8–15.
[26] S. Kase, T. Matsuo, Studies on melt spinning. II. Steady-state and transient solutions of fundamental equations compared with experimental results, J. Appl. Polym. Sci., 11 (1967) 251–287.
[27] O. Ishizuka, K. Koyama, Crystallization of running filament in melt spinning of polypropylene, Polymer, 18 (1977) 913–918.
[28] W.L. Chou, M.C. Yang, Effect of take-up speed on physical properties and permeation performance of cellulose acetate hollow fibers, J. Membr. Sci., 250 (2005) 259–267.
[29] H. Matsuyama, T. Maki, M. Teramoto, K. Asano, Effect of polypropylene molecular weight on porous membrane formation by thermally induced phase separation, J. Membr. Sci., 204 (2002) 323–328.
[30] O. Miyawaki, A. Saito, T. Matsuo, K. Nakamura, Activity and activity coefficient of water in aqueous solutions and their relationships with solution structure parameters, Biosci. Biotechnol. Biochem., 61 (1997) 466–469.

Supplementary material

Table S1
Material properties used to simulate the spinning of HFMs with nitrogen as core gas

Material properties	Value
ρ_d^0 = the density of the DBP calculated as constant (Kg/m^3)	9.05×10^2
ρ_o = spinline densities calculated as constant (Kg/m^3)	9.52×10^2
M_q = the molecular weight of the air	28.0
ΔH_d^{vap}(DBP) = the evaporation enthalpy of DBP (J/g)	$-0.37T + 467.85$
C_{pi} = core gas specific heat capacity as constant (kJ/(kg·K))	1.007
C_{po} = spinline specific heat capacity as constant (kJ/(kg·K)	2.47
χ = the interaction parameter	$-3.71 + 1{,}760.9/T$

Table S2
Process conditions used to simulate the spinning of HFMs with nitrogen as core gas

Process conditions	Value
$R_o(0)$ = spinneret outer radius (mm)	4.0
$R_i(0)$ = spinneret inner radius (mm)	2.4
w_o = the mass flow rates of drop (kg/s)	1.9
w_i = the mass flow rates of core gas (kg/s)	8.3×10^{-4}
$\overline{P}_i$ = initial core gas gauge pressure (KPa)	200
P_{atm} = the ambient air pressure (KPa)	101.3
v_L = take-up velocity (m/s)	0.075
T_q = the air temperature (K)	303.15
v_q = the air velocity (m/s)	0

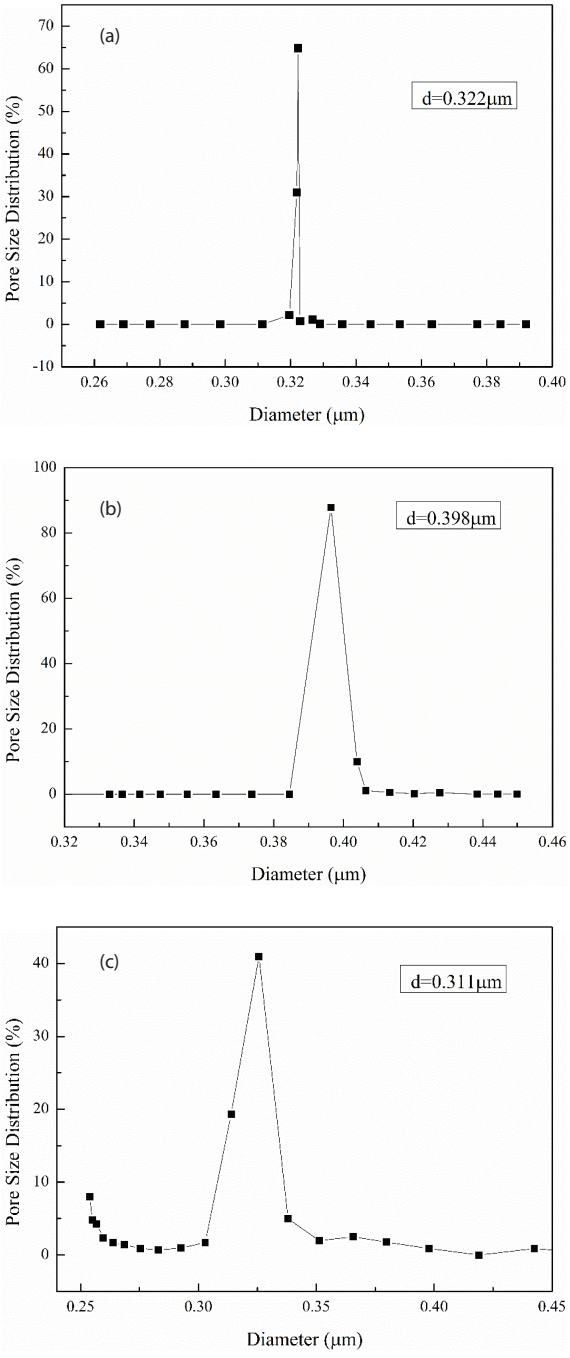

Fig. S1. Pore size distribution of HFMs under different spinning temperatures. (a) The pore size distribution of membrane under T = 408.15 K, (b) the pore size distribution of membrane under T = 421.15 K and (c) the pore size distribution of membrane under T = 434.15 K.